
INTERPRETABLE DIMENSIONALITY REDUCTION BY FEATURE PRESERVING MANIFOLD APPROXIMATION AND PROJECTION

Yang Yang
 Frazer Institute
 University of Queensland
 yang.yang1@uq.edu.au

Hongjian Sun
 Frazer Institute
 University of Queensland
 hongjian.sun@uq.edu.au

Jialei Gong
 Frazer Institute
 University of Queensland
 j.gong@uq.edu.au

Yali Du
 King's College London
 yali.du@kcl.ac.uk

Di Yu
 Frazer Institute
 University of Queensland
 di.yu@uq.edu.au

November 18, 2022

ABSTRACT

Nonlinear dimensionality reduction lacks interpretability due to the absence of source features in low-dimensional embedding space. We propose an interpretable method featMAP to preserve source features by tangent space embedding. The core of our proposal is to utilize local singular value decomposition (SVD) to approximate the tangent space which is embedded to low-dimensional space by maintaining the alignment. Based on the embedding tangent space, featMAP enables the interpretability by locally demonstrating the source features and feature importance. Furthermore, featMAP embeds the data points by anisotropic projection to preserve the local similarity and original density. We apply featMAP to interpreting digit classification, object detection and MNIST adversarial examples. FeatMAP uses source features to explicitly distinguish the digits and objects and to explain the misclassification of adversarial examples. We also compare featMAP with other state-of-the-art methods on local and global metrics.

1 Introduction

Nonlinear dimensionality reduction methods are ubiquitously applied for visualization and preprocessing high-dimensional data in machine learning [1, 2, 3, 4, 5, 6, 7, 8]. These methods assume that the intrinsic dimension of the underlying manifold is much lower than the ambient dimension of the real-world data [9, 10, 11]. Based on approximating the manifold by k nearest neighbour (k NN) graph, nonlinear dimensionality reduction projects data from high to low-dimensional space and retains the topological structure of original data.

While nonlinear dimensionality reduction is effective for visualizing high-dimensional data, one major weakness is lacking interpretability of the reduced-dimension results [8]. The reduced dimensions of nonlinear dimensionality reduction have no specific meaning, compared with linear methods like Principal Component Analysis (PCA) where the dimensions of the embedding space represent the directions of the largest variance of original data. Particularly, nonlinear dimensionality reduction focuses on preserving distance between observations and thereby loses source feature information in the embedding space, resulting in failing to illustrate feature loadings that linear methods such as PCA can provide to explain the feature contribution in each dimension.

In this paper, we seek to improve the interpretability of nonlinear dimensionality reduction. In addition to preserving the local topological structure between observations in the embedding space, we aim to incorporate the source features to devise an interpretable nonlinear dimensionality reduction method. The feature information is encoded in the column space of data, and we use the tangent space to locally depict the column space [12, 13]. The intuition of employing tangent space originates from the anisotropic density observation on a manifold such that some curves passing through a

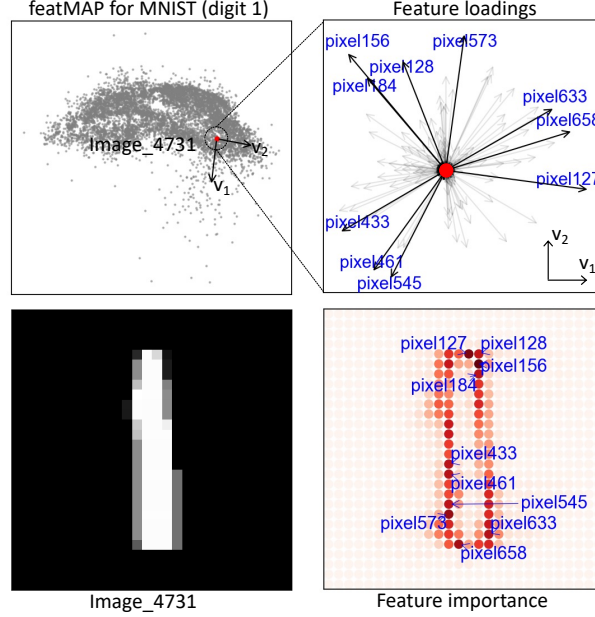


Figure 1: FeatMAP preserving source features. FeatMAP embeds the digit 1 group of MNIST to two-dimensional space (top-left). One randomly selected data point (in red) is associated with the embedding tangent space ($\text{span}(v_1, v_2)$) showing the source features (top-10 annotated) of every pixel (top-right). The feature importance computed by the feature loadings is mapped to the selected image (bottom-right), detecting the digit edge.

point in the manifold are flat while some through the same point are steep, indicating that the feature variation diverges in different directions. This equivalence class of tangent curves forms the tangent space which retains source feature information.

We propose **feature preserving manifold approximation and projection** (featMAP) to maintain both the pairwise distance on the manifold and the source features on tangent space. We first approximate the manifold topological structure by k NN graph [14, 15] and compute the tangent space by applying singular value decomposition (SVD) to the local nearest neighbours. The column space of SVD spans the basis for tangent space [12, 13]. The tangent spaces of two near data points are connected by parallel transport which is estimated as orthogonal transformation between the bases of tangent space [12]. We refer to the orthogonal transformation as alignment. In addition, the tangent space at one data point is associated with a k NN point cloud, whose radius is determined by the singular values of SVD. This local point cloud forms a hyperellipsoid demonstrating the anisotropic density. For dimensionality reduction, we first embed the tangent space by preserving the alignment between tangent spaces. We achieve this by depicting the alignment with cosine distance and minimizing the difference of cosine distance distribution between high and low-dimensional space. Based on the embedding tangent space, we project the data points to maintain pairwise distance by minimizing the difference of distance distribution in original and embedding space. We also preserve the anisotropic density by maximizing the correlation of local (hyper)ellipsoid radius between high and low-dimensional space.

The embedding tangent space by featMAP provides a frame to illustrate the source features. Figure 1 depicts an example of embedding MNIST (digit 1 group) dataset. The embedding coordinate of a randomly selected data point is associated with a local frame showing the source features and feature importance. To summarize, we make the following contributions:

- We propose featMAP, an interpretable nonlinear dimensionality reduction method that preserves source features and local similarity.
- We evaluate featMAP on digit and object data. FeatMAP utilizes feature information to successfully explain the digit classification and object detection.
- We apply featMAP to MNIST adversarial examples to explicitly show that the adversarial attack changes the feature importance, which fools the LeNet classifier.

In the following sections, we first discuss the related works before delving into the proposed method, followed by experiments on interpreting digit classification, object detection and MNIST adversarial examples, and comparing with the state-of-the-art methods on local and global metrics.

2 Related Work

The interpretability of nonlinear dimensionality reduction is missing to design and evaluate the embedding methods [16, 17, 18, 19]. Linear methods like PCA naturally possess the interpretability by explicitly showing source features [20]. Limited research has been conducted to address the interpretability of nonlinear dimensionality reduction. Liu *et al.* [16] proposed to understand the link of embedding dimensions and the original ones as a trade-off between interpretability and the intrinsic structure of the embedding. Bibai and Frénay [21] introduced to solve the interpretability problem by explaining the low-dimensional axes [22, 23] and analysing the data points position in scatter plot [24]; they further pointed out that the dimensionality reduction is interpretable if the embedding data points can be understood by high-dimensional features. Recently, Wu *et al.* [25] applied subspace projection to solving interpretable kernel dimensionality reduction. Bibal *et al.* [26] adapted local interpretable model-agnostic explanations to locally explain t-SNE. Bardos *et al.* [27] introduced a model-agnostic technique for local explanation of dimensionality reduction. Our approach aims to incorporate source features in embedding to locally illustrate feature importance and interpret the reduced-dimension results.

Nonlinear dimensionality reduction is claimed to better preserve distance and neighbourhood information in the projected manifold [28, 7, 8]. The current state-of-the-art manifold learning methods such as t-SNE [7], LargeVIs [29] and UMAP [8] create the low-dimensional embedding related to the SNE framework [30, 31, 32] which relies on constructing and embedding k NN graph to approximate the underlying manifold. Recently, several methods have attempted to improve the manifold learning methods based on exploiting topological structures. TriMAP [33] used 2-simplex structure and constructed triple constraints to improve global accuracy. PaCMAP [34] considered multi-hop structure to keep both local and global properties. DensMAP [35] computed the radius of local neighbourhood area to maintain the density of high-dimensional data. h-NNE [36] applied a hierarchy built on nearest neighbour graph to preserving multi-level grouping properties of original data. SpaceMAP [37] used space expansion to match the high and low-dimensional space. CO-SNE [38] extended t-SNE from Euclidean space to hyperbolic space. However, these methods lack interpretability due to the absence of source features in the embedding results.

Our approach belongs to the paradigm of manifold learning. Besides maintaining the manifold topological structure, we preserve the source features in tangent space [6, 12] and enable the interpretability of dimensionality reduction by locally understanding source features in embedding tangent space. This provides us with a highly effective and interpretable dimensionality reduction method.

3 The featMAP method

We present featMAP to preserve both manifold structure and source features in low-dimensional space. We first characterise the manifold topological structure by k NN graph and compute the tangent space by local SVD, then we embed the tangent space by preserving alignment between tangent spaces, and project the data points along the embedding tangent space to low-dimensional space. In the following sections, we elaborate on each step and validate the proposed methods. Figure 2 illustrates the framework of the method.

3.1 Topological space and feature space approximation

We follow the manifold assumption that data points $\{x_1, \dots, x_m\}^1 \subset \mathbb{R}^n$ lie on a d -dimensional Riemannian manifold \mathcal{M}^d embedded in \mathbb{R}^n with the intrinsic dimension $d \ll n$. For each data point x_i , \mathcal{M}^d has a tangent space $T_{x_i}\mathcal{M}$ that includes all vectors at x_i that are tangent to the manifold. Let $\{f_1, \dots, f_n\}$ denote the basis of the data points, which spans source feature space.

We first depict the manifold structure by weighted k NN graph (Figure 2) which approximates the geodesic distance on the manifold [15]. Let (X, E) denote the k NN graph, where $X = \{x_1, \dots, x_m\}$ are the data points and E the set of edges (i, j) . The edge weight P_{ij} of the k NN graph is calculated by the probability distribution on original data [8] as

$$\begin{aligned}\tilde{P}_{j|i} &= \exp(-(\|x_i - x_j\| - dist_i)/\gamma_i) \\ P_{ij} &= \tilde{P}_{j|i} + \tilde{P}_{i|j} - \tilde{P}_{j|i}\tilde{P}_{i|j}\end{aligned}\tag{1}$$

¹Vectors of lower-case letters refer to column vectors.

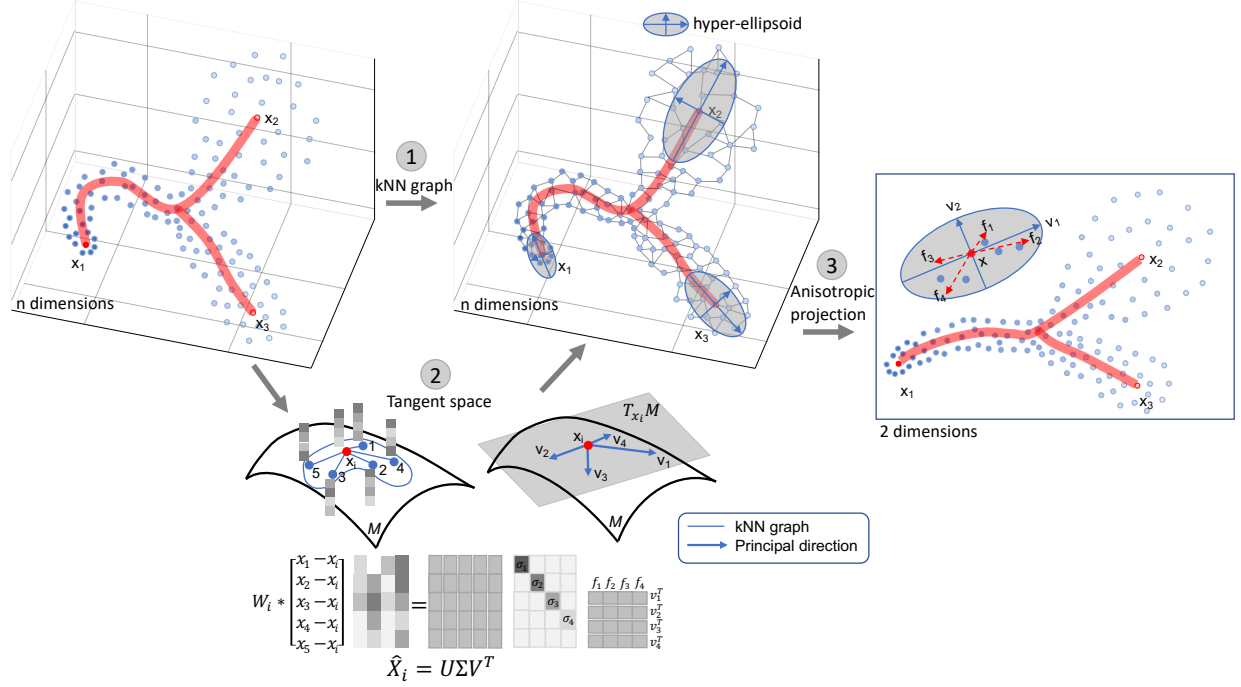


Figure 2: The framework of featMAP. With n -dimensional data (top-left) as input, featMAP first constructs the topological space by k NN graph (step 1, top-middle), followed by compute the tangent space by local SVD (step 2, bottom-middle) and embed the tangent space to preserve alignment (Figure 3). Along the embedding tangent space, featMAP applies anisotropic projection (step 3) to embedding the data to low-dimensional space (right), which locally retains the source features in embedding tangent space. Data points with darker blue indicate denser patterns, and vice versa.

where γ_i is adaptive for each i corresponding to the length-scale and $dist_i$ is the distance from x_i to its nearest neighbour. Note that small distance $\|x_i - x_j\|$ between data points i and j induces large similarity P_{ij} .

Based on the k NN graph capturing the topological structure, we retrieve the important features of the data points X . Obviously, the feature information is encoded in the column space of X , and the majority of information exists in the principal components [39]. Meanwhile, the features are not evenly distributed on the manifold because of curvature: some area on manifold presents plane surface, while some bends more sharply, thus we locally calculate principal components of the column space and extract important features.

Given a data point x_i , we center its k nearest neighbours as $X_i = [x_{i1} - x_i, \dots, x_{ik} - x_i]^T \in \mathbb{R}^{k \times n}$. Next, we construct the weight matrix as $W_i = \text{diag}(\sqrt{P_{ii_1}}, \dots, \sqrt{P_{ii_k}}) \in \mathbb{R}^{k \times k}$. Recall that P_{ij} is the edge weight of k NN graph in Equation (1). We assign larger weight to closer neighbours.

To locally derive the principal components around data point x_i , we apply singular value decomposition (SVD)² to $\hat{X}_i = W_i X_i$ and get

$$\hat{X}_i = U_i \Sigma_i V_i^T \quad (2)$$

where the singular values $\Sigma_i = \text{diag}(\sigma_{i1}, \dots, \sigma_{ik})$ are in decreasing order and the corresponding right eigenvectors $V_i = [v_{i1}, \dots, v_{ik}]$ span the column space of \hat{X}_i (Figure 2). The right eigenvectors V_i approximate the tangent space $T_{x_i}\mathcal{M}$ by the following theorem.

Theorem 3.1 ([12, 13]) *The right eigenvectors $V_i = [v_{i1}, \dots, v_{ik}]$ by SVD on \hat{X}_i approximately represent an orthonormal basis for the tangent space $T_{x_i}\mathcal{M}$.*

²In practice, k is small (e.g. 15), and the extra time cost for SVD is tolerable.

The decomposition in Equation (2) illustrates the feature loadings by $v_{il}^T = [v_{il}^{f_1}, \dots, v_{il}^{f_n}]$ on the l -th principal direction (Figure 2). We keep the largest d singular values³ and the corresponding right eigenvectors, and define the feature importance score for data point x_i as follows:

Definition 3.1 (Feature importance) *The feature importance for data point x_i in tangent space $T_{x_i}\mathcal{M}$ is defined as*

$$\|f_h^i\| = \left(\sum_{l=1}^d |v_{il}^{f_h}|^2 \right)^{\frac{1}{2}}, \quad h = 1, \dots, n. \quad (3)$$

The feature importance of source feature f_h is the l_2 -norm of the corresponding column vector in V_i^T , which locally characterises the feature variability around data point x_i on the manifold; features with larger scores are more variable in the ambient space.

The definition of feature importance shows that the tangent space locally retains the source feature information. For different data points x_i and x_j , the feature importance is separately calculated on the tangent space $T_{x_i}\mathcal{M}$ and $T_{x_j}\mathcal{M}$. Intuitively, tangent space varies at different data points. The tangent spaces of two near data points are connected by parallel transport. We estimate the parallel transport by rotation between the bases of tangent space and refer to it as alignment [12]. Consider two near data points x_i and x_j with distance $d_{\mathcal{M}}(i, j)$ on the manifold in Figure 3. The orthonormal matrices V_i, V_j approximate the bases of tangent spaces $T_{x_i}\mathcal{M}$ and $T_{x_j}\mathcal{M}$, respectively. The transformation from x_i to x_j involves translation and rotation operation. We calculate the translation by distance $d_{\mathcal{M}}(i, j)$, and the rotation by optimal alignment O_{ij} which is

$$O_{ij} = \arg \min_{O \in O(d)} \|O - V_j V_i^T\|_F. \quad (4)$$

Numerically, the alignment O_{ij} is computed by the SVD of $V_j V_i^T = U' \Sigma' V'^T$ and $O_{ij} = U' V'^T$. We define the transformation as:

$$\begin{aligned} \Gamma_{i \rightarrow j} : T_{x_i}\mathcal{M} &\rightarrow T_{x_j}\mathcal{M} \\ X &\mapsto O_{ij}X + d_{\mathcal{M}}(i, j). \end{aligned} \quad (5)$$

The transformation $\Gamma_{i \rightarrow j}$ represents the connection of data points i and j on both topological space (by distance $d_{\mathcal{M}}(i, j)$) and tangent space (by alignment O_{ij}). The conventional nonlinear dimensionality reduction methods focus on the former connection by preserving pairwise distance [40, 7, 8], which succeed in maintaining the topological structure, whereas the tangent space is missing in these methods, resulting in no source features preserved in low-dimensional embedding space.

We aim to preserve the topological structure as well as tangent space to reveal source features in low-dimensional space. We first embed the tangent space by preserving the alignment (Equation (4)), followed by maintaining the local distance along the embedding tangent space in low-dimensional space.

3.2 Tangent space embedding

The feature space of data points $X = \{x_1, \dots, x_m\}$ is locally depicted by the tangent space $T_x\mathcal{M}$ (Definition 3.1). We project the tangent space to low-dimensional space by preserving the alignment between tangent spaces (Figure 3).

For each point x_i , the tangent space $T_{x_i}\mathcal{M}$ is estimated by the d largest right eigenvectors $V_i = [v_{i1}, \dots, v_{id}]$ in Equation (2). The overall tangent space $T_x\mathcal{M}$ is approximated as $V = [V_1; \dots; V_m] \in \mathbb{R}^{m \times n \times d}$, which is a 3-order tensor demonstrating m data points with $n \times d$ -dimensional feature space.

We consider the tensor embedding on tangent bundle $\mathcal{M} \times T_x\mathcal{M}$, where the topological structure of \mathcal{M} is calculated by k NN graph and tangent space $T_x\mathcal{M}$ is by local SVD. For two data points x_i and x_j with corresponding tangent space basis V_i and V_j respectively, we define the consistence degree [41] between the tangent spaces $T_{x_i}\mathcal{M}$ and $T_{x_j}\mathcal{M}$ as

$$\cos \Theta_{ij} = \frac{\langle V_i, V_j \rangle_F}{\|V_i\|_F \|V_j\|_F} \quad (6)$$

where $\langle V_i, V_j \rangle_F = \text{tr}(V_i V_j^T)$ denotes the Frobenius inner product and $\|\cdot\|_F$ is Frobenius norm. Equation (6) presents the cosine similarity between tangent space $T_{x_i}\mathcal{M}$ and $T_{x_j}\mathcal{M}$, which induces a general angle Θ_{ij} in Figure 3. Note that the above consistence degree quantitatively characterises the alignment in Equation (4). We define the probability distribution of the consistence degree on original tangent space as

$$\mathbf{P}_{j|i}(\Theta) = \exp(-(|1 - \cos \Theta_{ij}| - \text{dist}'_i)/\gamma'_i) \quad (7)$$

³The intrinsic dimension d is locally estimated as the number of singular values that account for most data variability [12, 13].

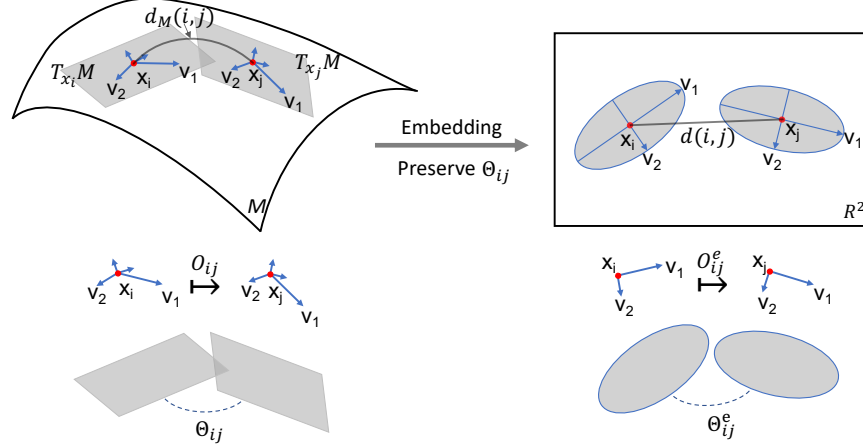


Figure 3: Tangent space embedding. The tangent spaces of original data points x_i and x_j are associated with basis vectors (v_1 and v_2 annotated, on the left); the transformation from i to j consists of translation by geodesic distance $d_M(i, j)$ and rotation O_{ij} with the general angle Θ_{ij} (bottom-left). The embedding tangent space (on the right) is computed by preserving the rotation angle Θ_{ij} .

where $1 - \cos \Theta_{ij}$ is the cosine distance and we set normalization to $\mathbf{P}_{j|i}(\Theta)$ similar as Equation (1) to get $\mathbf{P}_{ij}(\Theta)$. We focus on preserving the pairwise cosine distance of tangent spaces in low-dimensional embedding space.

Consider projecting the manifold to d' -dimensional space ($d' \leq d \ll n$). For each data point x_i , let $V_i^e = [v_{i1}^e, \dots, v_{id'}^e] \in \mathbb{R}^{d' \times d'}$ denote the embedding tangent space. Similarly, we define the cosine similarity between V_i^e and V_j^e as

$$\cos \Theta_{ij}^e = \frac{\langle V_i^e, V_j^e \rangle_F}{\|V_i^e\|_F \|V_j^e\|_F} \quad (8)$$

with the angle Θ_{ij}^e in Figure 3. We aim to learn the tangent space embedding $V^e = \{V_1^e, \dots, V_m^e\}$ to make V^e have similar distribution on cosine distance to original space by Equation (7). For the probability distribution on the embedding tangent space, we inherit the heavy-tailed distribution from [7, 8] as:

$$\mathbf{Q}_{ij}(\Theta^e) = (1 + ad_{ij}^{2b}(s, t))^{-1} \quad (9)$$

where $d_{ij} = 1 - \cos \Theta_{ij}^e$ represents the cosine distance between the embedding tangent spaces V_i^e and V_j^e and a, b are shape parameters.

To preserve the alignment in embedding tangent space, we minimize the difference between \mathbf{P} and \mathbf{Q} by Kullback–Leibler divergence:

$$KL(\mathbf{P}||\mathbf{Q}) = - \sum_{ij} \mathbf{P}_{ij}(\log \mathbf{P}_{ij} - \log \mathbf{Q}_{ij}), \quad (10)$$

and we optimize the embedding feature space $V^e = [V_1^e; \dots; V_m^e]$ to minimize the loss function by stochastic gradient descent (SGD).

The embedding tangent space $V^e = [V_1^e; \dots; V_m^e]$ equips the topological space with a frame for source features (on the right of Figure 2). The feature loadings (dashed arrows) are derived from the top d' eigenvectors of original tangent space V , and the feature importance is illustrated by the arrows' length.

The embedding tangent space V^e also presents the directions along which the data points are locally distributed in low-dimensional space. Note that the directions of tangent space $T_{x_i}\mathcal{M}$ are weighted by the singular values $[\sigma_{i1}, \dots, \sigma_{id}]$ (Equation (2)), which forms a hyperellipsoid showing anisotropic density (top-middle of Figure 2). Thus, we will project the original data points along the local weighted directions to preserve the anisotropic density in low-dimensional space.

3.3 Anisotropic projection

In this section, we compute the d' -dimensional ($d' \leq d \ll n$) embedding points $Y = \{y_1, \dots, y_m\}$ under the frame of embedding tangent space V^e . We have constructed the tangent space $V^e = [V_1^e; \dots; V_m^e] \in \mathbb{R}^{m \times d' \times d'}$ in low-dimensional embedding space (Figure 3), and each local space V_i^e is associated with weights by the singular values

$\Sigma_i^e = \text{diag}(\sigma_{i1}, \dots, \sigma_{id'})$. This tangent space locally portrays an anisotropic projection of data points $X = \{x_1, \dots, x_m\}$ to low-dimensional space.

We first calculate the 1-skeleton topological structure in low-dimensional space by the heavy-tailed distribution [8]:

$$Q_{ij} = (1 + a\|y_i - y_j\|^{2b})^{-1} \quad (11)$$

where $\|y_i - y_j\|$ denotes the (Euclidean) distance in embedding space, and a, b are shape parameters. We preserve the distance by minimizing the difference between distribution Q_{ij} and P_{ij} (Equation (1)) by cross-entropy loss

$$CE(P||Q) = - \sum_{ij} P_{ij} \log Q_{ij} + (1 - P_{ij}) \log(1 - Q_{ij}) \quad (12)$$

Consider the low-dimensional data points y_i with the embedding frame $V_i^e = [v_{i1}^e, \dots, v_{id'}^e] \in \mathbf{R}^{d' \times d'}$. We center its k nearest neighbours as $Y_i = [y_{i1} - y_i, \dots, y_{ik} - y_i]^T \in \mathbf{R}^{k \times d'}$, and project Y_i to its tangent space V_i^e as $\hat{Y}_i = Y_i V_i^e$. For one of y_i 's neighbours, say y_j , the distance $\|y_i - y_j\|$ is invariant under the rotation V_i^e , which makes \hat{Y}_i fit Equation (11).

Recall that the original tangent space V_i with weight $\Sigma_i = \text{diag}(\sigma_{i1}, \dots, \sigma_{id})$ forms a hyperellipsoid (top-middle of Figure 2) with radius $R_{il}^o = \sigma_{il}^2, l = 1, \dots, d^4$. We reshape the embedding data points $\hat{Y}_i = Y_i V_i^e$ such that the volume of the point cloud \hat{Y}_i agrees with the original hyperellipsoid. The radius of \hat{Y}_i in direction v_{il}^e ($l = 1, \dots, d'$) is

$$R_{il}^e = \frac{1}{\sum_j Q_{ij}} \sum_j Q_{ij} \|(y_j - y_i) v_{il}^e\|^2, \quad (13)$$

where R_{il}^e ($l = 1, \dots, d'$) results from the anisotropic projection. The local hyperellipsoid volume of original and embedding space is $c(d) \prod_{l=1}^d R_{il}^o = c(d') \prod_{l=1}^{d'} R_{il}^e$, where c denotes a constant related to dimensions. We reframe this equation by logarithm and get

$$r_{i1}^o + \dots + r_{id'}^o + c = r_{i1}^e + \dots + r_{id'}^e \quad (14)$$

where $r_{il}^o = \log R_{il}^o$ and $r_{il}^e = \log R_{il}^e$. To preserve the volume in embedding space, it is sufficient to set $r_{il}^e = \beta r_{il}^o + \alpha, i = 1, \dots, m$ in the l -th ($l = 1, \dots, d'$) direction. We measure the goodness of fitting this relationship by correlation coefficient

$$\text{Corr}(r_l^o, r_l^e) = \frac{\text{Cov}(r_l^o, r_l^e)}{(\text{Var}(r_l^o) \text{Var}(r_l^e))^{1/2}} \quad (15)$$

and for all directions, we have

$$\text{Corr}(r^o, r^e) = \sum_{l=1}^{d'} \text{Corr}(r_l^o, r_l^e) \quad (16)$$

We combine the loss function for preserving 1-skeleton structure (Equation (12)) and correlation coefficient for anisotropic density (Equation (19)) to get the overall loss function

$$\mathcal{L} = CE(P||Q) - \lambda \text{Corr}(r^o, r^e) \quad (17)$$

where λ determines the relative importance of anisotropic density preservation. We use SGD to minimize the above loss function to get d' -dimensional embedding coordinates $Y = \{y_1, \dots, y_m\}$.

Therefore, the embedding coordinates $Y = \{y_1, \dots, y_m\}$ by the anisotropic projection not only preserve the topological structure of local similarity and density, but also encapsulate the embedding tangent space V^e which locally demonstrates the source features (on the right of Figure 2).

Training. The calculation details for SGD are in Supplementary. In practice, we set the (hyper)parameters same as UMAP [8] including number of neighbours, number of iterations and the 'min-dist' parameter. There are two additional parameters: the weight $\lambda \leq 0$ for the anisotropic density preservation and the fraction $q \in [0, 1]$ of iterations that considers tangent space embedding. We use 15 neighbours, 500 epochs, $q = 0.3$ and $\lambda = 0.5$. We include tuning of λ in Supplementary (Fig. 11).

4 Experiments

We evaluate featMAP in interpreting MNIST digit classification as well as Fashion MNIST and COIL-20 object detection by using source features in embedding space. We also apply featMAP to interpreting MNIST adversarial examples, showing that our method featMAP uses feature importance to explicitly explain the misclassification after adversarial attack. In addition, we show that featMAP maintains the original density by anisotropic projection. In the end, we compare featMAP with state-of-the-art algorithms by local and global structure preservation metrics.

⁴We use squared distance (variance) because of better empirical performance.

4.1 Datasets and evaluation metrics

We perform the evaluation on various datasets including standard MNIST [42], Fashion MNIST [43], COIL-20 [44], Cifar10 [45], single cell RNA-seq [46], and MNIST adversarial examples [47]. We compare with representative methods for dimensionality reduction and visualization, including t-SNE [7], Fit-SNE [48], h-NNE [36], UMAP [8], triMAP [33], PaCMAP [34], densMAP [35] and spaceMAP [37] in terms of both local and global structure preservation [49, 34]. Local structure preservation metrics include k NN accuracy, trustworthiness [50] and continuity [51]. Global structure preservation metrics cover Shepard goodness, normalized stress [52] and triplet centroid accuracy [34]. The details to calculate these metrics are found in [49, 34].

4.2 Results

4.2.1 FeatMAP preserving source features

We demonstrate that featMAP enables interpretable dimensionality reduction by preserving source features on MNIST digit classification as well as Fashion MNIST and COIL-20 object detection. Figure 4 clearly shows the clusters of different digit groups using featMAP. We randomly choose one data point from each cluster and show the feature importance as saliency map for the corresponding images. We find that the pattern by feature importance explicitly detects the edge of each digit. Similarly, we apply featMAP to datasets Fashion MNIST and COIL-20 in Figure 5. The important features succeed in detecting the objects of different categories in both datasets. We also find that for COIL-20 dataset, the rotation patterns (the lighter red curves) are revealed in the saliency map, which originates from generating the dataset COIL-20 by rotating those objects with a fixed camera [44].

We further illustrate the interpretability of featMAP by showing the feature loadings and feature importance in Figure 1. Specifically, we annotate the top-10 most important pixel features. These pixels mainly appear in the corner angles of the digit object, indicating that these features locally dominate the image. This phenomenon is also observed in the saliency map of digits in Figure 4.

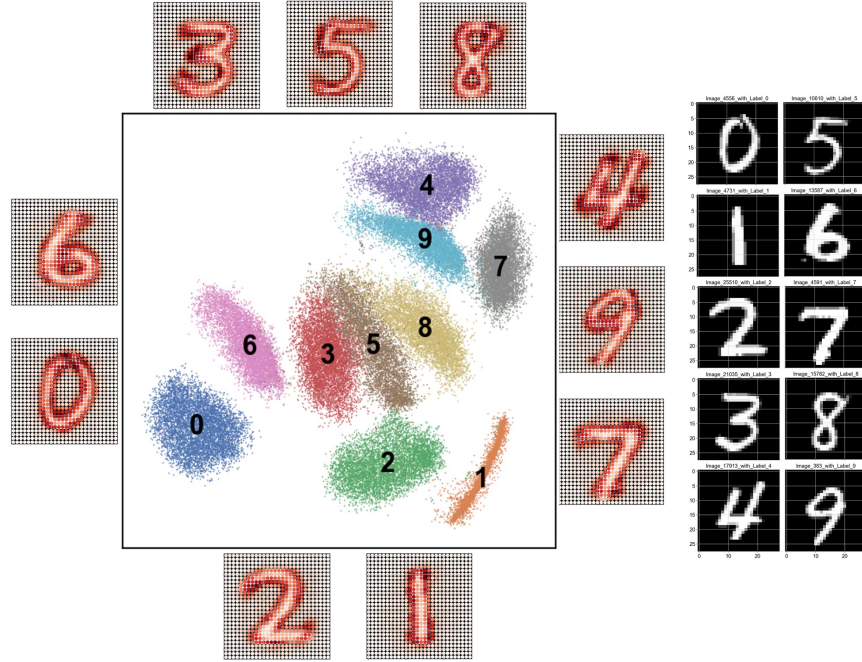


Figure 4: FeatMAP on MNIST showing feature importance. FeatMAP embeds MNIST to 2-dimensional space with 10 different clusters (left). Digit images are randomly selected from each cluster illustrating the feature importance with corresponding original images (right). Darker red means larger feature importance.

4.2.2 FeatMAP interpreting adversarial examples

We show that featMAP interprets MNIST adversarial examples by explaining the misclassification after adversarial attack. We use Fast Gradient Sign Attack (FGSM) [47] to synthesize fake images of MNIST with $\epsilon = 0.3$ and prediction

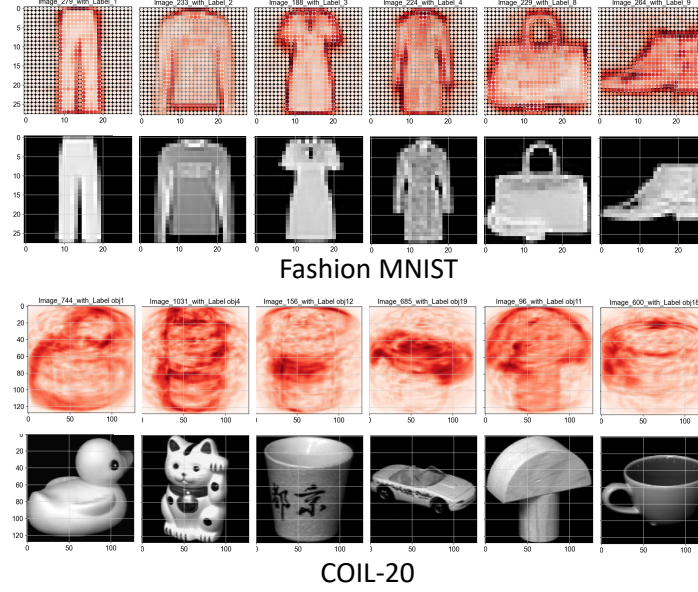


Figure 5: FeatMAP on Fashion MNIST and COIL-20 showing feature importance. For each dataset, the upper part is the saliency map by feature importance and the bottom are the original images.

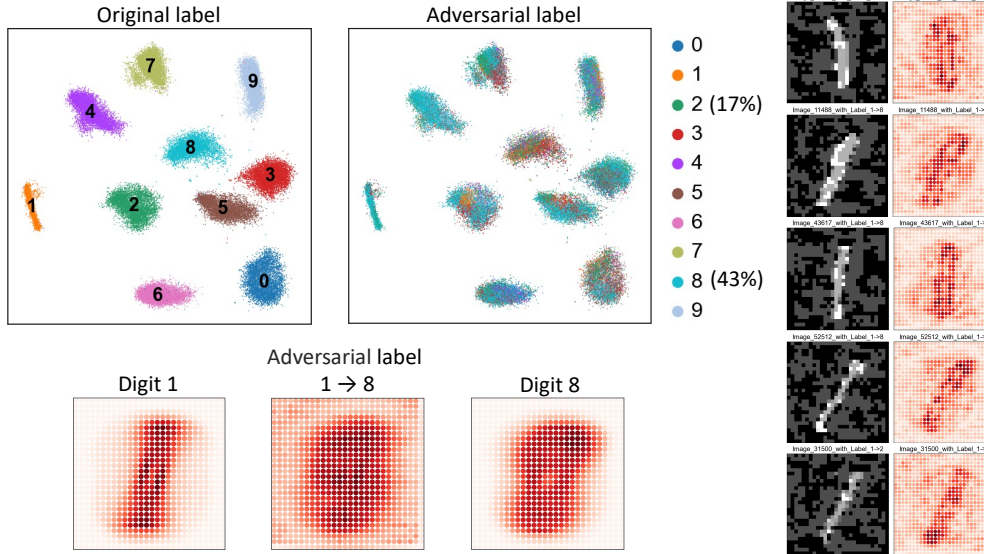


Figure 6: FeatMAP on MNIST adversarial examples. FeatMAP embeds MNIST adversarial examples to 2-dimensional space with original and adversarial labels (top-left). Five randomly selected adversarial examples from original digit 1 group are shown on the right. The bottom-left shows the average feature importance of adversarial examples misclassified from 1 to 8 and the corresponding digits 1 and 8 in original data before attack.

accuracy 0.08, to fool the classifier LeNet [53]. Formally, the adversarial example $x' \in \mathbb{R}^n$ satisfies $\|x' - x\| \leq \epsilon$, where x is the original image, and the predicted label $f(x') \neq f(x)$. The results are included in Figure 6 and Supplementary Figure 8.

We plot the adversarial examples by featMAP in Figure 6. The top-left part shows the original and adversarial labels. We find that the clustering structures of the adversarial examples are quite similar to original clusters in Figure 4, because the adversarial examples fall within x 's ϵ -neighbour ball ($\epsilon = 0.3$) which locally resembles the topological structure of original examples. FGSM successfully fools the classifier with 43% data misclassified as digit 8. We

randomly select five images from the cluster with original label digit 1, and illustrate the adversarial images with feature importance on the right of Figure 6. The adversarial images are identified as digit 1 by the naked eye, while the saliency map reveals other important features besides the edge features of digit 1. We average the feature importance of the adversarial examples misclassified from digit 1 to 8, and compare it with the original average feature importance of digit 1 and 8 (bottom-left in Figure 6). We find that the important feature patterns in adversarial examples are more similar to the pattern in original label 8 than 1, which evidently explains the misclassification after attack.

4.2.3 FeatMAP preserving density

We illustrate that featMAP maintains original data density in two-dimensional plot. We apply featMAP to the digit 1 group of MNIST dataset and plot the correlation of local radius between embedding and original space. FeatMAP presents larger local radius correlation than UMAP (in Supplementary Figure 9), indicating that featMAP performs better in local density preservation. Particularly, we cluster the dataset and find that the subgroup (in brown colour) is significantly more sparse in featMAP than UMAP in Figure 7. We claim that featMAP correctly reveals this sparse pattern because featMAP shows positive correlation of local radius between embedding and original space. We further demonstrate the digit images from this subgroup in Supplementary Figure 10, which exhibit diverse handwritten patterns and agree with the sparse pattern in featMAP.

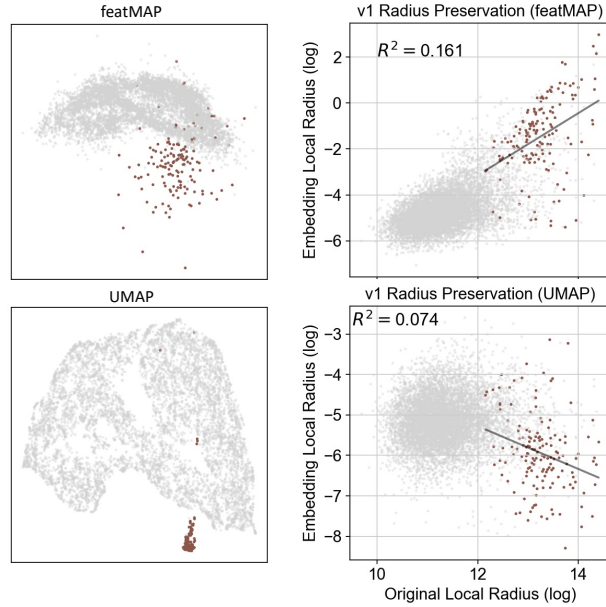


Figure 7: FeatMAP on MNIST (digit 1) showing density preservation. For one subgroup (colour in brown), featMAP (top) preserves the local radius against UMAP (bottom) by positive correlation between embedding and original local radius; featMAP correctly illustrates the sparse pattern compared to UMAP.

4.3 Quantitative comparison with state-of-the-art

We compare featMAP with representative dimensionality reduction methods. The two-dimensional visualization plots are in Supplementary Figure 12. We report the quantitative comparison results in Table 1. FeatMAP illustrates comparable results on both local and global metrics.

5 Conclusion

We propose featMAP enabling the interpretability of nonlinear dimensionality reduction. FeatMAP preserves the source features in low-dimensional embedding space, which facilitates explaining the embedding by high-dimensional features. Specifically, we embed the tangent space to locally construct a frame showing source features, thus explaining the reduced-dimension results by feature importance. FeatMAP also maintains the anisotropic density in two-dimensional plot, which further enhances the interpretability of visualization. The experiments on digit classification, object detection and MNIST adversarial examples demonstrate that featMAP produces interpretable dimensionality reduction

Table 1: Quantitative comparison. M_t , M_c and M_k indicate the local metrics as trustworthiness, continuity and k NN accuracy, respectively; M_s , M_σ and M_{ct} denote the global metrics as Shepard goodness, normalized stress and centroid triplet accuracy, respectively.

Experiments		t-SNE	Fit-SNE	h-NNE	UMAP	triMAP	PaCMAP	densMAP	spaceMAP	featMAP
MNIST	M_t	0.98	0.99	0.96	0.96	0.95	0.95	0.93	0.95	0.89
	M_c	0.97	0.97	0.93	0.97	0.96	0.96	0.97	0.96	0.97
	M_k	0.97	0.97	0.96	0.97	0.96	0.97	0.96	0.97	0.97
Fashion	M_t	0.99	0.99	0.95	0.98	0.97	0.97	0.96	0.97	0.94
MNIST	M_c	0.99	0.99	0.95	0.99	0.99	0.98	0.98	0.98	0.98
	M_k	0.82	0.84	0.84	0.79	0.76	0.77	0.76	0.80	0.77
COIL-20	M_t	1.00	1.00	0.98	0.99	0.99	0.99	0.98	0.98	0.94
	M_c	0.99	0.99	0.97	1.00	0.99	1.00	0.99	0.99	0.99
	M_k	0.95	0.94	0.89	0.87	0.82	0.84	0.92	0.86	0.92
Cifar10	M_t	0.93	0.93	0.83	0.84	0.85	0.84	0.80	0.90	0.80
	M_c	0.92	0.92	0.76	0.94	0.94	0.93	0.92	0.94	0.94
	M_k	0.82	0.84	0.84	0.79	0.76	0.77	0.31	0.76	0.76
RNA-seq	M_t	0.99	0.99	0.96	0.96	0.95	0.95	0.93	0.98	0.89
	M_c	0.97	0.97	0.94	0.97	0.96	0.96	0.97	0.97	0.97
	M_k	0.66	0.71	0.69	0.64	0.63	0.62	0.62	0.67	0.62

(a) Local metrics

Experiments		t-SNE	Fit-SNE	h-NNE	UMAP	triMAP	PaCMAP	densMAP	spaceMAP	featMAP
MNIST	M_s	0.39	0.41	0.20	0.39	0.17	0.28	0.51	0.26	0.43
	$1-M_\sigma$	0.95	0.97	1.00	1.00	0.96	0.99	0.99	0.93	0.99
	M_{ct}	0.65	0.68	0.70	0.69	0.67	0.71	0.70	0.69	0.70
Fashion	M_s	0.61	0.68	0.40	0.61	0.66	0.60	0.65	0.66	0.66
MNIST	$1-M_\sigma$	0.96	0.97	1.00	0.99	0.96	0.99	0.99	0.93	0.99
	M_{ct}	0.70	0.78	0.75	0.82	0.85	0.80	0.82	0.81	0.82
COIL-20	M_s	0.52	0.60	0.65	0.18	0.30	0.39	0.25	0.21	0.29
	$1-M_\sigma$	0.99	0.99	0.99	1.00	0.99	1.00	1.00	0.97	1.00
	M_{ct}	0.74	0.75	0.73	0.60	0.65	0.69	0.58	0.63	0.59
Cifar10	M_s	0.65	0.64	0.24	0.68	0.74	0.72	0.78	0.61	0.74
	$1-M_\sigma$	0.99	0.99	1.00	1.00	0.98	1.00	1.00	0.97	1.00
	M_{ct}	0.93	0.93	0.67	0.92	0.91	0.92	0.92	0.86	0.93
RNA-seq	M_s	0.44	0.41	0.18	0.39	0.17	0.28	0.50	0.67	0.45
	$1-M_\sigma$	0.95	0.97	1.00	1.00	0.96	0.99	0.99	0.73	0.99
	M_{ct}	0.74	0.78	0.60	0.79	0.84	0.79	0.79	0.76	0.80

(b) Global metrics

results, which boost explaining the classification and feature detection. Our method to preserve features by tangent space embedding provides a plug-in module for manifold learning. In future work, we expect to extend our feature preserving paradigm by tangent space embedding to other nonlinear dimensionality reduction methods to enable the interpretability. Another future work is to apply featMAP to real-world images and biological gene expression data to strengthen interpreting the classification and feature detection.

References

- [1] Joshua B Tenenbaum, Vin de Silva, and John C Langford. A global geometric framework for nonlinear dimensionality reduction. *science*, 290(5500):2319–2323, 2000.
- [2] Sam T Roweis and Lawrence K Saul. Nonlinear dimensionality reduction by locally linear embedding. *science*, 290(5500):2323–2326, 2000.
- [3] Zhenyue Zhang and Jing Wang. Mlle: Modified locally linear embedding using multiple weights. *Advances in neural information processing systems*, 19, 2006.
- [4] David L Donoho and Carrie Grimes. Hessian eigenmaps: Locally linear embedding techniques for high-dimensional data. *Proceedings of the National Academy of Sciences*, 100(10):5591–5596, 2003.
- [5] Mikhail Belkin and Partha Niyogi. Laplacian eigenmaps for dimensionality reduction and data representation. *Neural computation*, 15(6):1373–1396, 2003.
- [6] Zhenyue Zhang and Hongyuan Zha. Principal manifolds and nonlinear dimensionality reduction via tangent space alignment. *SIAM journal on scientific computing*, 26(1):313–338, 2004.
- [7] Laurens Van der Maaten and Geoffrey Hinton. Visualizing data using t-sne. *Journal of machine learning research*, 9(11), 2008.
- [8] Leland McInnes, John Healy, and James Melville. Umap: Uniform manifold approximation and projection for dimension reduction. *arXiv preprint arXiv:1802.03426*, 2018.
- [9] Elizaveta Levina and Peter Bickel. Maximum likelihood estimation of intrinsic dimension. *Advances in neural information processing systems*, 17, 2004.
- [10] Phillip Pope, Chen Zhu, Ahmed Abdelkader, Micah Goldblum, and Tom Goldstein. The intrinsic dimension of images and its impact on learning. *arXiv preprint arXiv:2104.08894*, 2021.
- [11] John Wright and Yi Ma. *High-dimensional data analysis with low-dimensional models: Principles, computation, and applications*. Cambridge University Press, 2022.
- [12] Amit Singer and H-T Wu. Vector diffusion maps and the connection laplacian. *Communications on pure and applied mathematics*, 65(8):1067–1144, 2012.
- [13] Uzu Lim, Vidit Nanda, and Harald Oberhauser. Tangent space and dimension estimation with the wasserstein distance. *arXiv preprint arXiv:2110.06357*, 2021.
- [14] Franco P Preparata and Michael I Shamos. *Computational geometry: an introduction*. Springer Science & Business Media, 2012.

- [15] Wei Dong, Charikar Moses, and Kai Li. Efficient k-nearest neighbor graph construction for generic similarity measures. In *Proceedings of the 20th international conference on World wide web*, pages 577–586, 2011.
- [16] Shusen Liu, Dan Maljovec, Bei Wang, Peer-Timo Bremer, and Valerio Pascucci. Visualizing high-dimensional data: Advances in the past decade. *IEEE transactions on visualization and computer graphics*, 23(3):1249–1268, 2016.
- [17] Alfredo Vellido, José David Martín-Guerrero, and Paulo JG Lisboa. Making machine learning models interpretable. In *ESANN*, volume 12, pages 163–172. Bruges, Belgium, 2012.
- [18] Benoît Frénay and Bruno Dumas. Information visualisation and machine learning: Characteristics, convergence and perspective. In *24th European Symposium on Artificial Neural Networks, Computational Intelligence and Machine Learning, ESANN 2016*, pages 623–628. i6doc. com publication, 2016.
- [19] Bruno Dumas, Benoît Frénay, and John Lee. Interaction and user integration in machine learning for information visualisation. In *26th European Symposium on Artificial Neural Networks, Computational Intelligence and Machine Learning (ESANN 2018)*, pages 97–104. i6doc. com. publ., 2018.
- [20] Karl Ruben Gabriel. The biplot graphic display of matrices with application to principal component analysis. *Biometrika*, 58(3):453–467, 1971.
- [21] Adrien Bibal and Benoit Frénay. Measuring quality and interpretability of dimensionality reduction visualizations. In *Safe Machine Learning Workshop at ICLR*, 2019.
- [22] Adrien Bibal, Rebecca Marion, and Benoît Frénay. Finding the most interpretable mds rotation for sparse linear models based on external features. In *ESANN*, 2018.
- [23] Rebecca Marion, Adrien Bibal, and Benoît Frénay. Bir: A method for selecting the best interpretable multidimensional scaling rotation using external variables. *Neurocomputing*, 342:83–96, 2019.
- [24] Mike Sips, Boris Neubert, John P Lewis, and Pat Hanrahan. Selecting good views of high-dimensional data using class consistency. In *Computer Graphics Forum*, volume 28, pages 831–838. Wiley Online Library, 2009.
- [25] Chieh Wu, Jared Miller, Yale Chang, Mario Sznajer, and Jennifer Dy. Solving interpretable kernel dimension reduction. *arXiv preprint arXiv:1909.03093*, 2019.
- [26] Adrien Bibal, Viet Minh Vu, Géraldine Nanfack, and Benoît Frénay. Explaining t-sne embeddings locally by adapting lime. In *ESANN*, pages 393–398, 2020.
- [27] Avraam Bardos, Ioannis Mollas, Nick Bassiliades, and Grigorios Tsoumakas. Local explanation of dimensionality reduction. *arXiv preprint arXiv:2204.14012*, 2022.
- [28] Ingwer Borg and Patrick JF Groenen. *Modern multidimensional scaling: Theory and applications*. Springer Science & Business Media, 2005.
- [29] Jian Tang, Jingzhou Liu, Ming Zhang, and Qiaozhu Mei. Visualizing large-scale and high-dimensional data. In *Proceedings of the 25th international conference on world wide web*, pages 287–297, 2016.
- [30] Geoffrey E Hinton and Sam Roweis. Stochastic neighbor embedding. *Advances in neural information processing systems*, 15, 2002.
- [31] Jan Niklas Böhm, Philipp Berens, and Dmitry Kobak. Attraction-repulsion spectrum in neighbor embeddings. *Journal of Machine Learning Research*, 23(95):1–32, 2022.
- [32] Sebastian Damrich, Jan Niklas Böhm, Fred A Hamprecht, and Dmitry Kobak. Contrastive learning unifies t-sne and umap. *arXiv preprint arXiv:2206.01816*, 2022.
- [33] Ehsan Amid and Manfred K Warmuth. Trimap: Large-scale dimensionality reduction using triplets. *arXiv preprint arXiv:1910.00204*, 2019.
- [34] Yingfan Wang, Haiyang Huang, Cynthia Rudin, and Yaron Shaposhnik. Understanding how dimension reduction tools work: An empirical approach to deciphering t-sne, umap, trimap, and pacmap for data visualization. *J. Mach. Learn. Res.*, 22(201):1–73, 2021.
- [35] Ashwin Narayan, Bonnie Berger, and Hyunghoon Cho. Assessing single-cell transcriptomic variability through density-preserving data visualization. *Nature Biotechnology*, 39(6):765–774, 2021.
- [36] Saquib Sarfraz, Marios Koulakis, Constantin Seibold, and Rainer Stiefelhagen. Hierarchical nearest neighbor graph embedding for efficient dimensionality reduction. In *Proceedings of the IEEE/CVF Conference on Computer Vision and Pattern Recognition*, pages 336–345, 2022.
- [37] Xinrui Zu and Qian Tao. Spacemap: Visualizing high-dimensional data by space expansion. In *International Conference on Machine Learning*, pages 27707–27723. PMLR, 2022.

- [38] Yunhui Guo, Haoran Guo, and Stella X Yu. Co-sne: Dimensionality reduction and visualization for hyperbolic data. In *Proceedings of the IEEE/CVF Conference on Computer Vision and Pattern Recognition*, pages 21–30, 2022.
- [39] Ian T Jolliffe and Jorge Cadima. Principal component analysis: a review and recent developments. *Philosophical Transactions of the Royal Society A: Mathematical, Physical and Engineering Sciences*, 374(2065):20150202, 2016.
- [40] Ronald R Coifman, Stephane Lafon, Ann B Lee, Mauro Maggioni, Boaz Nadler, Frederick Warner, and Steven W Zucker. Geometric diffusions as a tool for harmonic analysis and structure definition of data: Diffusion maps. *Proceedings of the national academy of sciences*, 102(21):7426–7431, 2005.
- [41] Tingquan Deng, Dongsheng Ye, Rong Ma, Hamido Fujita, and Lvnan Xiong. Low-rank local tangent space embedding for subspace clustering. *Information Sciences*, 508:1–21, 2020.
- [42] Yann LeCun. The mnist database of handwritten digits. <http://yann.lecun.com/exdb/mnist/>, 1998.
- [43] Han Xiao, Kashif Rasul, and Roland Vollgraf. Fashion-mnist: a novel image dataset for benchmarking machine learning algorithms. *arXiv preprint arXiv:1708.07747*, 2017.
- [44] Sameer A Nene, Shree K Nayar, Hiroshi Murase, et al. Columbia object image library (coil-20). 1996.
- [45] Alex Krizhevsky, Geoffrey Hinton, et al. Learning multiple layers of features from tiny images. 2009.
- [46] Can Liu, Andrew J Martins, William W Lau, Nicholas Rachmaninoff, Jinguo Chen, Luisa Imberti, Darius Mostaghimi, Danielle L Fink, Peter D Burbelo, Kerry Dobbs, et al. Time-resolved systems immunology reveals a late juncture linked to fatal covid-19. *Cell*, 184(7):1836–1857, 2021.
- [47] Ian J Goodfellow, Jonathon Shlens, and Christian Szegedy. Explaining and harnessing adversarial examples. *arXiv preprint arXiv:1412.6572*, 2014.
- [48] Laurens Van Der Maaten. Accelerating t-sne using tree-based algorithms. *The Journal of Machine Learning Research*, 15(1):3221–3245, 2014.
- [49] Mateus Espadoto, Rafael M Martins, Andreas Kerren, Nina ST Hirata, and Alexandru C Telea. Toward a quantitative survey of dimension reduction techniques. *IEEE transactions on visualization and computer graphics*, 27(3):2153–2173, 2019.
- [50] Jarkko Venna and Samuel Kaski. Local multidimensional scaling. *Neural Networks*, 19(6-7):889–899, 2006.
- [51] Jarkko Venna and Samuel Kaski. Visualizing gene interaction graphs with local multidimensional scaling. In *ESANN*, volume 6, pages 557–562, 2006.
- [52] Paulo Joia, Danilo Coimbra, Jose A Cuminato, Fernando V Paulovich, and Luis G Nonato. Local affine multidimensional projection. *IEEE Transactions on Visualization and Computer Graphics*, 17(12):2563–2571, 2011.
- [53] Yann LeCun, Léon Bottou, Yoshua Bengio, and Patrick Haffner. Gradient-based learning applied to document recognition. *Proceedings of the IEEE*, 86(11):2278–2324, 1998.

6 Supplementary

6.1 Stochastic gradient descent (SGD) for anisotropic projection

We use anisotropic projection to embed the data points into low-dimensional space. To apply SGD to optimizing the embedding coordinates, we calculate the derivative of the loss function

$$\mathcal{L} = CE(P||Q) - \lambda Corr(r^o, r^e). \quad (18)$$

The core of the anisotropic projection lies in optimizing the Pearson correlation between the local radius in original and embedding space. We first calculate the gradient of this correlation regarding the embedding coordinates for optimization. We rewrite the correlation as follows:

$$Corr(r^o, r^e) = \sum_{l=1}^{d'} \frac{Cov(r_l^o, r_l^e)}{(Var(r_l^o) Var(r_l^e))^{1/2}} \quad (19)$$

where $r_l^o = \{r_{il}^o\}_{i=1}^m = \{\log R_{il}^o\}_{i=1}^m$ and $r_l^e = \{r_{il}^e\}_{i=1}^m = \{\log R_{il}^e\}_{i=1}^m$ in the l -th principal direction of original and embedding spaces respectively. We set $z_{ij} = y_j - y_i$ and rewrite r_{il}^e as

$$\begin{aligned} r_{il}^e &= \log R_{il}^e = \log \frac{1}{\sum_j Q_{ij}} \sum_j Q_{ij} \|(y_j - y_i) v_{il}^e\|^2 \\ &= \log \frac{1}{\sum_j Q_{ij}} \sum_j Q_{ij} \|z_{ij} v_{il}^e\|^2, \end{aligned} \quad (20)$$

and

$$Q_{ij} = \frac{1}{1 + a(y_j - y_i)^{2b}} = [1 + a(z_{ij}^T z_{ij})^b]^{-1} \quad (21)$$

Let

$$\rho_{e,o}^{(l)} = \frac{\text{Cov}(r_l^o, r_l^e)}{(\text{Var}(r_l^o) \text{Var}(r_l^e))^{1/2}}, \quad (22)$$

be the correlation in the l -th direction. The derivative of $\rho_{e,o}^{(l)}$ with respect to z_{ij} is

$$\frac{\partial \rho_{e,o}^{(l)}}{\partial z_{ij}} = \text{Var}(r_l^o)^{-1/2} \left[\frac{\partial \text{Cov}(r_l^o, r_l^e)}{\partial z_{ij}} \text{Var}(r_l^e)^{-1/2} - \frac{1}{2} \text{Cov}(r_l^o, r_l^e) \text{Var}(r_l^e)^{-3/2} \frac{\partial \text{Var}(r_l^e)}{\partial z_{ij}} \right] \quad (23)$$

Therefore, the gradient of the correlation in Equation (16) in the l -th principal direction regarding the embedding coordinates y_i is

$$\Delta_{y_i} \text{Corr}^{(l)}(r^o, r^e) = \sum_{j \neq i} \frac{\partial \rho_{e,o}^{(l)}}{\partial z_{ij}} \frac{\partial z_{ij}}{\partial y_i} \quad (24)$$

We further compute the derivative of the variance and covariance in Equation (23). To simplify the notation, we set $\mu_l^e = \mathbb{E}[r_l^e]$ and center the original local radius as $r_{il}^o := \log R_{il}^o - m^{-1} \sum_{i=1}^m \log R_{il}^o$. The gradient in Equation (23) (l omitted) is calculated as

$$\begin{aligned} \frac{\partial \rho_{e,o}^{(l)}}{\partial z_{ij}} &= \text{Var}(r^o)^{-\frac{1}{2}} \left\{ \frac{1}{m-1} (r_i^o \frac{\partial r_i^e}{\partial z_{ij}} + r_j^o \frac{\partial r_j^e}{\partial z_{ij}}) \text{Var}(r_l^e)^{-\frac{1}{2}} \right. \\ &\quad - \frac{1}{m-1} \text{Cov}(r^o, r^e) \text{Var}(r^e)^{-\frac{3}{2}} [(r_i^e - \mu^e) \frac{\partial r_i^e}{\partial z_{ij}} \\ &\quad \left. + (r_j^e - \mu^e) \frac{\partial r_j^e}{\partial z_{ij}}] \right\}, \end{aligned} \quad (25)$$

and

$$\frac{\partial r_i^e}{\partial z_{ij}} = \frac{\tilde{Q}_{ij}^2 W_i}{R_i^e} [(1 + a(z_{ij}^T z_{ij})^b - 2ab(z_{ij}^T z_{ij})^{b-1} z_{ij} z_{ij}^T) 2v_i v_i^T z_{ij}] + \tilde{Q}_{ij}^2 W_i * 2ab(z_{ij}^T z_{ij})^{b-1} z_{ij} \quad (26)$$

where $W_i = \sum_{s=1} (1 + a(z_{is}^T z_{is})^b)^{-1}$ and $\tilde{Q}_{ij} = W_i^{-1} (1 + a(z_{ij}^T z_{ij})^b)^{-1}$.

Next, we compute the gradient of the cross-entropy $CE(P||Q)$ (similar to UMAP [8]). The cross-entropy loss function is

$$\mathcal{L}_{ce} = CE(P||Q) = - \sum_{ij} P_{ij} \log Q_{ij} + (1 - P_{ij}) \log(1 - Q_{ij}) \quad (27)$$

and its gradient with respect to z_{ij} is

$$\frac{\partial \mathcal{L}_{ce}}{\partial z_{ij}} = -[P_{ij} \frac{\partial \log Q_{ij}}{\partial z_{ij}} + (1 - P_{ij}) \frac{\partial \log(1 - Q_{ij})}{\partial z_{ij}}] \quad (28)$$

where $\frac{\partial \log Q_{ij}}{\partial z_{ij}} = \frac{-2ab(z_{ij}^T z_{ij})^{b-1} z_{ij}}{1 + a(z_{ij}^T z_{ij})^b}$ and $\frac{\partial \log(1 - Q_{ij})}{\partial z_{ij}} = \frac{1}{z_{ij}^T z_{ij}} \frac{2bz_{ij}}{1 + (z_{ij}^T z_{ij})^b}$.

The attractive term $P_{ij} \log Q_{ij}$ is optimized by randomly drawing an edge (i, j) by distribution P , which means that the edge (i, j) is selected with probability $\frac{P_{ij}}{\sum_{i \neq j} P_{ij}}$, followed by calculating the gradient $\frac{\partial \log Q_{ij}}{\partial z_{ij}}$. The repulsive term is estimated by uniformly at random choosing a set of points S adjacent to the given point x_i and computing $\frac{1}{|S|} \sum_{l \in S} \frac{\partial \log(1 - Q_{il})}{\partial z_{il}}$.

Combine the gradient of cross-entropy in Equation (28) and local radius correlation in Equation (25). The gradient for an edge (i, j) at each iteration of the SGD in the l -th principal direction is

$$\Delta_{y_i} \mathcal{L}|_{(i,j)} = -\left[\frac{\partial \log Q_{ij}}{\partial z_{ij}} - \frac{1}{|S|} \sum_{l \in S} \frac{\partial \log(1 - Q_{il})}{\partial z_{il}} + \lambda \frac{Z}{mP_{ij}} \frac{\partial \rho_{e,o}^{(l)}}{\partial z_{ij}}\right] \frac{\partial z_{ij}}{\partial y_i}, \quad (29)$$

where $Z = \sum_{(i,j)} P_{ij}$ and $\frac{mP_{ij}}{Z}$ is the normalization factor considering the edge is chosen with probability $\frac{P_{ij}}{Z}$.

In addition, we compute the gradient in Equation (25) at the start of each epoch. We achieve this by calculating $W_i = \sum_{s=1} Q_{is}$, the local radius r_{il}^e , the variance and covariance terms in the beginning of each epoch, regarding them as fixed for all the edges to be updated during that epoch.

6.2 Stochastic Gradient Descent (SGD) for tangent space embedding

The key of tangent space embedding is to preserve the alignment between tangent spaces. We depict the alignment by the general angle between two tangent spaces, which induces the cosine distance of tangent spaces. We further model the probability distribution of cosine distance in original and embedding space respectively, and minimize the difference of distribution by KL divergence to maintain the alignment in embedding space.

In practice, we borrow the framework of t-SNE or UMAP to compute the embedding tangent space. Specifically, we flat the tensor of tangent space in original space and feed it to t-SNE as input. We set the parameter *distance* as *cosine*. The output is normalized to get the embedding tangent space.

6.3 FeatMAP interpreting adversarial examples

We illustrate how the digits 1 are misclassified to the other labels in Figure 8. The saliency map illustrates the average feature importance. The feature importance pattern in the middle is more similar to the right than the left, indicating that the adversarial attack FGSM alters the feature importance and fools the LeNet classifier.

6.4 FeatMAP preserving original density

FeatMAP presents larger local radius correlation than UMAP in Figure 9. We cluster the data (digit 1 in MNIST) on the right of Figure 9 and find that the subgroup 5 (in brown colour) is significantly more sparse in featMAP than UMAP. We further demonstrate the digit images from this subgroup in Figure 10, which exhibit diverse handwritten patterns and agree with the sparse pattern in featMAP.

6.5 Hyperparameter tuning

We demonstrate the tuning of the hyperparameter λ in the loss function of featMAP in Figure 11. The parameter $\lambda = 0$ corresponds to UMAP. With the increasing of λ , featMAP performs better in preserving the local anisotropic density with the local radius correlation getting larger, while the clusters in the two-dimensional plot are not clearly separable when λ is large. Consider the trade-off between the local density preservation and clusters visualization, we set the parameter λ as 0.5.

6.6 Comparing featMAP with other state-of-the-art

We apply the state-of-the-art nonlinear dimensionality reduction methods to the benchmark datasets to visualize the data in Figure 12. FeatMAP illustrates the density preservation as well as densMAP [35].

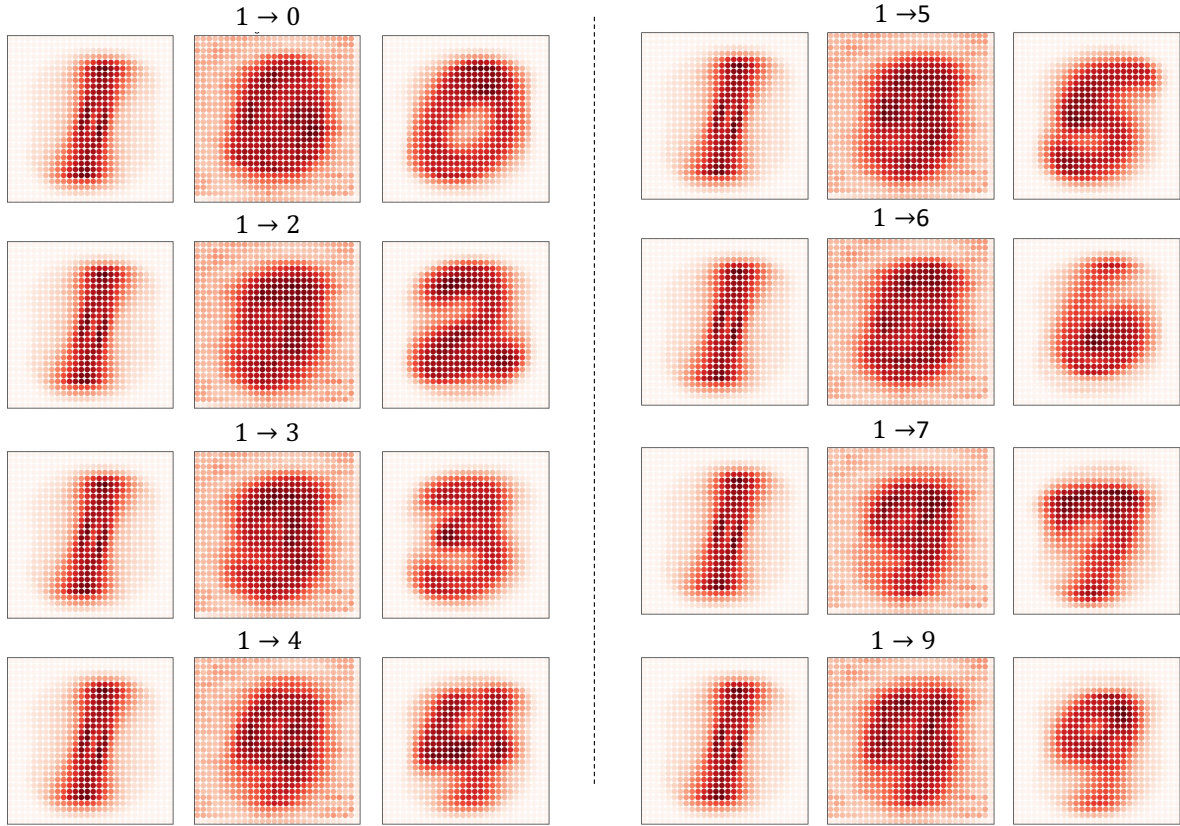


Figure 8: Average feature importance of the adversarial examples and the corresponding original data. For the original digits 1, we list all the corresponding adversarial examples with average feature importance in the middle. The left is the original digit 1 and the right is the original digit with the label same as the corresponding adversarial label.

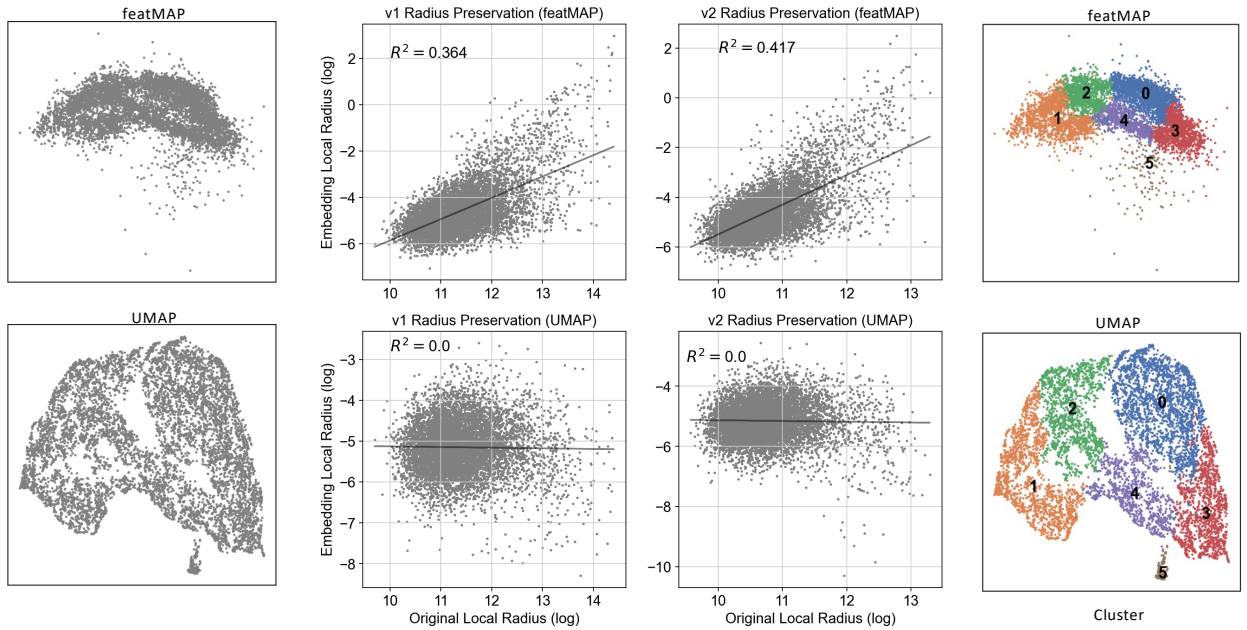


Figure 9: FeatMAP preserving the original density. FeatMAP and UMAP are applied to digit 1 group of MNIST (left). The middle is the scatter plot of embedding local radius against original local radius, along with the straight line of linear regression showing the correlation of local radius between embedding and original space. The right illustrates the clusters on both featMAP and UMAP.

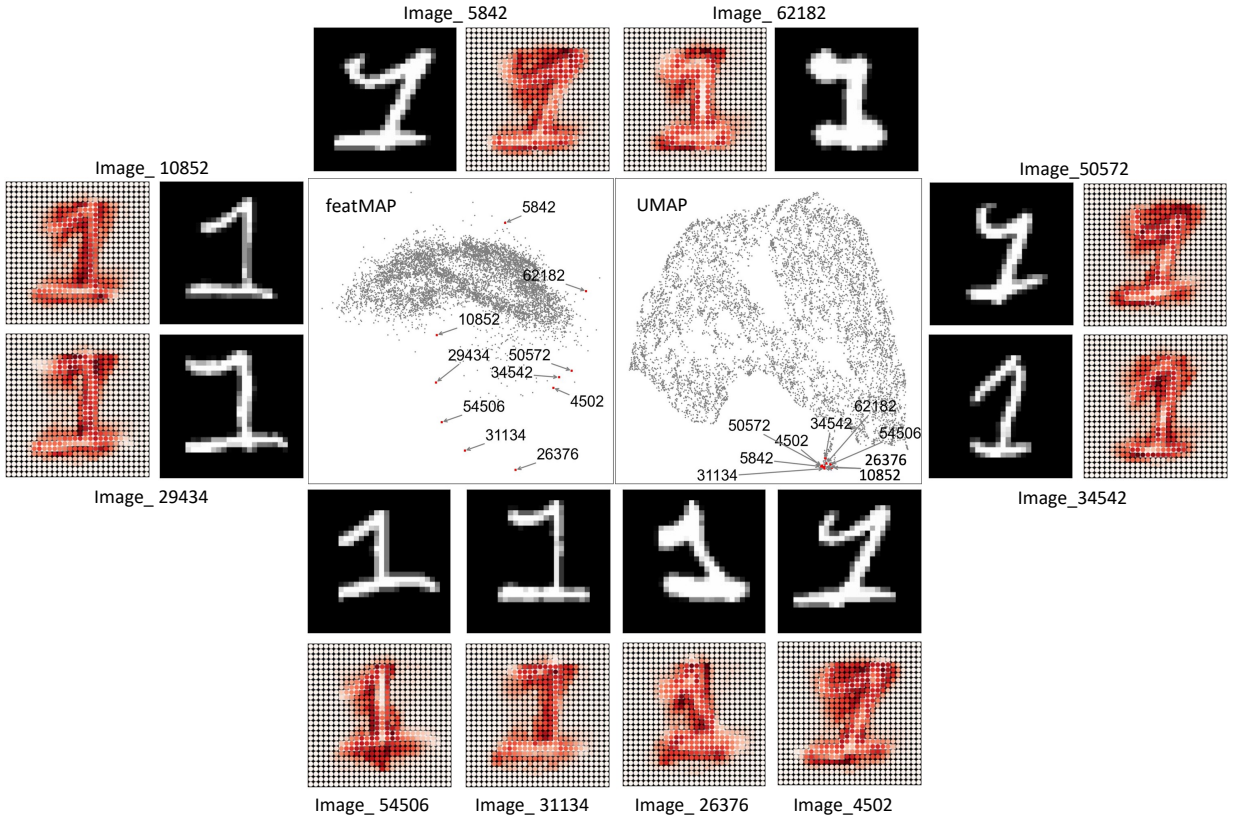


Figure 10: Handwritten digit images from the sparse subgroup of featMAP. 10 data points are randomly selected from the subgroup 5 in Figure 9 with the corresponding digit images.

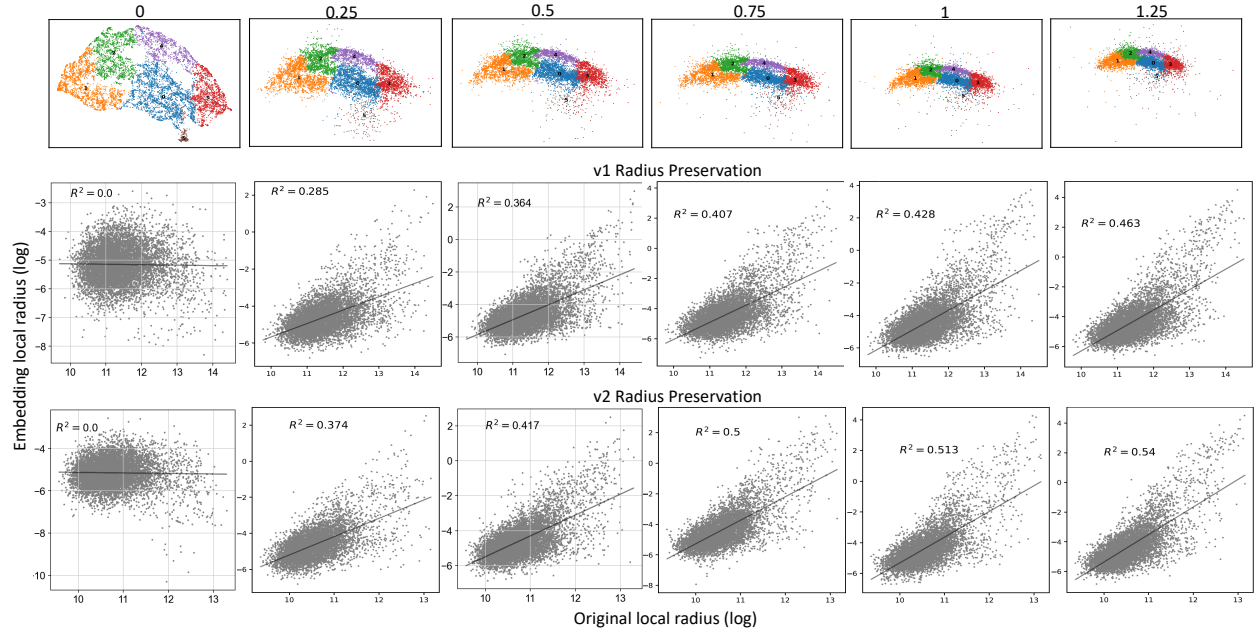


Figure 11: The tuning of hyperparameter λ . The hyperparameter λ in featMAP is set from 0 to 1.25 with two-dimensional plot and local radius correlation.

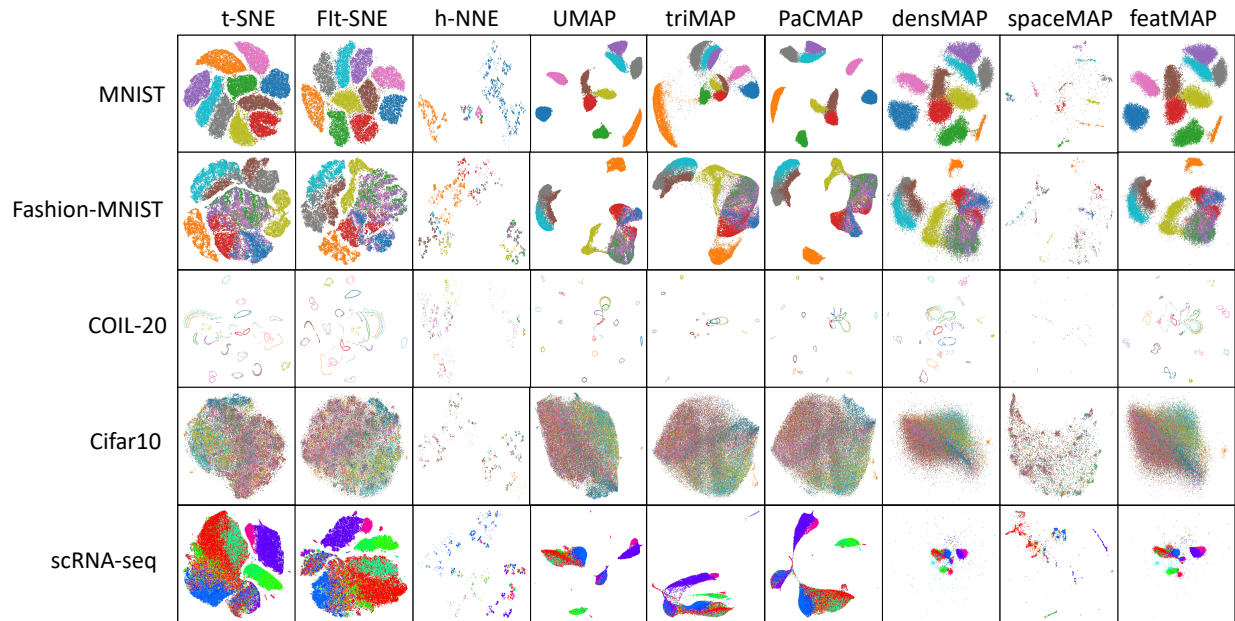


Figure 12: Visualization of multiple datasets by the state-of-the-art nonlinear dimensionality reduction methods.